ROYAL SOCIETY OF CHEMISTRY

PAPER

Check for updates

Revealing the oxygen reduction reaction activity origin of single atoms supported on g-C$_3$N$_4$ monolayers: a first-principles study†

Huan Niu, [ID] [a] Xiting Wang,[a] Chen Shao,[a] Yuanshuang Liu,[b] Zhaofu Zhang [ID] *[c] and Yuzheng Guo*[a]

Herein, the potential of single transition metal atoms (TM, from Ti to Au) supported on g-C$_3$N$_4$ (TM/g-C$_3$N$_4$) for the oxygen reduction reaction (ORR) was investigated by first-principles calculations. It was demonstrated that the TM atoms can remain stable in the cavity of g-C$_3$N$_4$ and interact with the substrate *via* charge transfer from the TM atoms to g-C$_3$N$_4$. Among all the TM/g-C$_3$N$_4$ samples, Pd/g-C$_3$N$_4$ stands out with a low overpotential of 0.46 V, showing good performance for ORR; thus, it has great potential to replace the noble Pt catalyst. The ORR activity of TM/g-C$_3$N$_4$ is a function of ΔE_{*OH} (an energy descriptor). Furthermore, the d-band center and ICOHP (electronic structure descriptors) can quantitatively describe the variation trend of ΔE_{*OH} in addition to Bader charge analysis (a charge transfer descriptor). Considering the number of d orbital electrons and the electronegativity of TM, φ (an intrinsic descriptor) can be applied to predict and reveal the origin of the ORR activity. A bridge from intrinsic characteristics to electronic structures, to charge transfer, to electronic structures and then to adsorption energy has been established, which is conducive to better reveal the ORR activity origin and provide guidance for designing effective ORR electrocatalysts.

1. Introduction

With their advantages of high power density and small exhaust emissions, low-temperature fuel cells[1] can efficiently convert chemical energy into electric energy.[2] As a crucial process in fuel cells, the oxygen reduction reaction (ORR) demands efficient catalysts.[3] As conventional electrocatalysts, Pt-based materials are widely employed in ORR owing to their high activity.[4–7] However, the high cost, poor stability and low natural abundance of Pt greatly limit the practical applications of these materials. Hence, it is essential to find potential catalysts to decrease the use of Pt-based materials and improve their catalytic efficiency.[8–10]

Accordingly, single-atom catalysts (SACs) have gained ever-increasing interest since Pt/FeO$_x$ was prepared in 2011.[11] SACs refer to a series of supported metal catalysts, where a metal is monodispersed as a single atom supported on the surface or anchored in the skeleton, such as many metal oxides, including FeO$_x$,[11] Al$_2$O$_3$,[12] TiO$_2$,[13] and CeO$_2$.[14] It has become a new frontier in heterogeneous catalysis to maximize the use of active sites. However, the free energy of a metal increases as its sizes decrease. Therefore, it is critical to find proper supports possessing strong interaction with single metal atoms to prevent their aggregation.[15]

Benefiting from their high specific surface areas and weak van der Waals interactions, 2D materials have become one of the most advantageous candidates for supporting single metal atoms.[16] In the past years, 2D materials have been widely used as substrates, such as nitrogen-doped graphene (N-G),[17] graphdiyne (GDY),[18] C$_3$N,[19] and transition metal dichalcogenides (TMDs).[20] In addition, graphitic carbon nitride (g-C$_3$N$_4$), as an easy-to-synthesize and low-cost 2D material, has been used for the photocatalytic hydrogen evolution reaction (HER).[21,22] To anchor TM atoms, it is essential to create regular vacancies for graphene and h-BN, which is challenging in experiments. In contrast, g-C$_3$N$_4$ possesses evenly distributed holes, which provide abundant nitrogen coordinators with rich electron lone pairs to capture metal atoms in the ligands. Recently, various single transition metals supported on g-C$_3$N$_4$ (TM/g-C$_3$N$_4$) have been experimentally synthesized, such as Co,[23] Ni,[24] Ru,[25] Pd,[26] and Pt.[27] From a theoretical perspective, it has been found that TM/g-C$_3$N$_4$ can act as potential SACs for CO$_2$ reduction,[28] CO oxidation,[29] and the N$_2$ reduction reaction (NRR).[30] For the application of ORR, He *et al.*[31] and Chen *et al.*[32] reported that a single Pd atom supported on g-C$_3$N$_4$ showed high ORR activity. However, an all-around and

[a]School of Electrical Engineering, Wuhan University, Wuhan, Hubei 430072, China. E-mail: yguo@whu.edu.cn

[b]State Key Laboratory of Tribology, School of Mechanical Engineering, Tsinghua University, Beijing, 10084, China

[c]Department of Engineering, Cambridge University, Cambridge, CB2 1PZ, UK. E-mail: zz389@cam.ac.uk

† Electronic supplementary information (ESI) available. See DOI: 10.1039/d0ta00794c

This journal is © The Royal Society of Chemistry 2020

J. Mater. Chem. A, 2020, **8**, 6555–6563 | 6555

in-depth understanding of the origin of the ORR has not been achieved. Thus, it is well worth exploring whether Pd/g-C_3N_4 is the best ORR electrocatalyst among the TM/g-C_3N_4, what descriptor can properly describe and even predict the ORR activity of the different metal centres, and where the ORR activity originates from.

In this study, we comprehensively studied the 3d, 4d and 5d single transition metal atoms supported on a buckle g-C_3N_4 monolayer (TM = Ti, V, Cr, Mn, Fe, Co, Ni, Cu, Zr, Nb, Mo, Ru, Rh, Pd, Ag, Hf, W, Re, Ir, Pt, and Au) to investigate their stability, evaluate their ORR performance, establish proper descriptors, and reveal the origin of their ORR activity by first-principles calculations. The stability of TM supported on g-C_3N_4 was described by calculating the binding energy and cohesive energy. The overpotentials of all the TM/g-C_3N_4 were evaluated and Pd/g-C_3N_4 stood out with the lowest overpotential of 0.46 V. The relationship between the overpotential and the adsorption energy of OH (ΔE_{*OH}) was determined. With the help of the d band theory, pCOHP and Bader charge analysis, our work shed light on the accurate quantitative description of ORR activity trends. Considering the number of d orbital electrons and the electronegativity of TM, a descriptor φ was applied to predict the ORR activity, which revealed the origin of the ORR activity.

2. Computational details

We employed the spin-polarized density functional theory (DFT) method for all calculations, as implemented in the Vienna *ab initio* Simulation Package (VASP) code.[33] The projector-augmented-wave (PAW) basis set[34] was adopted to describe the ion–electron interaction with a cut-off energy of 520 eV. The Perdew–Burke–Ernzerhof (PBE) of the generalized gradient approximation (GGA) functional[35] was used to treat the exchange–correlation interaction. Γ-Centred $5 \times 5 \times 1$ and $11 \times 11 \times 1$ k-points grids were chosen for optimization and electronic structure calculations, respectively. The convergence tolerance of energy and force was 10^{-5} eV and 0.01 eV Å^{-1}. DFT+U calculation was performed with $U = 4.0$ eV and $J = 1.0$ eV to consider the Coulomb interaction effect on all the screened TM.[36,37] The similar magnetic ground states for the TM atoms (Fig. S1†) and similar adsorption energies of the ORR intermediates (Table S1†) indicate that the DFT method is acceptable in this work. The van der Waals interactions were described by the empirical correction in Grimme's scheme (DFT-D3).[38] A 20 Å thickness vacuum was inserted to eliminate the interaction induced by a periodic boundary condition. Bader charge population analysis was employed to analysis the charge population and electron transfer.[39] To evaluate the kinetic stability, the climbing image nudged elastic band (CI-NEB) method was used to calculate the diffusion energy barrier of the TM atoms on g-C_3N_4.[40] *Ab initio* molecular dynamics (AIMD) simulations were conducted to evaluate the thermodynamic stability of the catalysts.[41] We employed the projected crystal orbital Hamilton population (pCOHP) to reveal the interaction between TM/g-C_3N_4 and the ORR intermediates.[42–44] VASPKIT, a pre- and post-processing tool in the VASP code, was adopted to manage the electronic structures.[45]

The adsorption energies of the O_xH_y species ($\Delta E_{*O_xH_y}$) involved in the ORR (O_2, OOH, O, OH and H_2O) on the substrates were determined by[46]

$$\Delta E_{*O_xH_y} = E_{*O_xH_y} - E_* - \left(xE_{H_2O} - \frac{2x-y}{2}E_{H_2} \right) \quad (1)$$

where $E_{*O_xH_y}$, E_*, E_{H_2O} and E_{H_2} denote the total energy of the O_xH_y species adsorbed on the substrate, the g-C_3N_4 substrate, water molecule and hydrogen molecule, respectively. Specifically, the more negative the adsorption energy, the stronger the adsorption strength.

The free energies in the electrochemical reaction pathways were calculated based on the computational hydrogen electrode (CHE) model proposed by Nørskov and co-workers.[47] The change in the Gibbs free energy (ΔG) for each reaction step is given as follows:

$$\Delta G = \Delta E + \Delta ZPE - T\Delta S + \Delta U + \Delta pH \quad (2)$$

where ΔE can be directly obtained from DFT calculations, representing the total energy difference between the product and reactant. ΔZPE and $T\Delta S$ are the zero-point energy correction and the entropy change at room temperature (298.15 K), respectively. The results of ZPE and TS are listed in Table S2,† which are consistent with the previous study.[48] ΔpH is the free energy correction of pH, calculated by $\Delta pH = kT \ln 10 \times pH$, and the pH value is zero in this work. $\Delta eU = -eU$, where e and U are the number of electrons transferred and the applied electrode potential, respectively. The potential-determining step (PDS) is the step with the most unfavourable equilibrium potential. The theoretical overpotential η_{ORR} is defined as:

$$\eta_{ORR} = \max(\Delta G_1, \Delta G_2, \Delta G_3, \Delta G_4)/e + 1.23 \quad (3)$$

3. Results and discussion

3.1 Stability of TM supported on g-C_3N_4

As shown in Fig. 1a, the g-C_3N_4 monolayer has a buckle structure with a lattice constant of 6.95 Å, which is more stable and more reasonable than the planar model (Fig. S2†).[49,50] We focused on the TM embedded in the g-C_3N_4 cavity (Fig. 1b), which is a suitable site to stabilize TM atoms.[51] To comprehensively understand the effect of the TM centres on the ORR activity, a series of 3d, 4d, and 5d transition metals were considered, as shown in Fig. 1c.

With an increase in atomic number, the average bond length (d_{ave}) gradually increases, indicating protrusion from the cavity (Fig. 2a). The bond lengths between the TM atoms and neighboring N atoms are listed in Table S3.† The deviation degree (ε) between the TM atoms and the cavity centre can be defined as:

$$\varepsilon = \left(1 - \frac{d_{TM-N(min)}}{d_{TM-N(max)}} \right) \times 100\% \quad (4)$$

where $d_{TM-N(min)}$ and $d_{TM-N(max)}$ denote the minimum and maximum value of the TM–N bond lengths, respectively. As can be seen in Fig. 2b, the TM atoms may deviate from the cavity

6556 | *J. Mater. Chem. A*, 2020, **8**, 6555–6563

This journal is © The Royal Society of Chemistry 2020

Fig. 1 Top-view and side-view of g-C₃N₄ (a) without and (b) with a single transition metal atom embedded in the central cavity. (c) Transition metals (with the atomic number label) considered in this work.

center, consistent with the previous study.[29,52] Re, Ru, Rh, and Ir show a significant deviation, while V and Nb remain close to the centre of the cavity.

The strong binding can prevent the aggregation of single TM atoms on the substrate. The binding strength of the TM on the g-C₃N₄ monolayer was calculated to compare their structural stability. The binding energies (ΔE_{bind}) of the metal atoms on g-C₃N₄ and the TM bulk cohesive energy (ΔE_{coh}) are defined as

$$\Delta E_{bind} = E_{TM/g\text{-}C_3N_4} - E_{g\text{-}C_3N_4} - E_{TM\text{-single}} \quad (5)$$

$$\Delta E_{coh} = E_{TM/bulk}/N - E_{TM\text{-single}} \quad (6)$$

where N denotes the number of atoms in the TM bulk unit cell. $E_{TM/g\text{-}C_3N_4}$, $E_{g\text{-}C_3N_4}$, $E_{TM\text{-single}}$ and $E_{TM/bulk}$ are the total energy of g-C₃N₄ (with and without TM) and TM (in vacuum and in bulk), respectively. If $\Delta E_{bind} < 0$, it is expected that the single TM atom can be tightly embedded in g-C₃N₄. According to Fig. 2c, the binding energies are all negative, ranging from −6.93 to −0.77 eV. With an increase in atomic number, the binding strength decreases in each period, opposite to the variation of d_{ave}. The Zr atom shows the strongest binding of −6.93 eV with a short d_{ave} of 2.34 Å, while the Au atom processes the weakest binding of −0.77 eV with a long d_{ave} of 2.58 Å.

Actually, clustering on the surface is unfavourable where $\Delta E_{bind} - \Delta E_{coh}$ is negative. However, even if the value is positive, the TM atoms are stable on the substrate when the diffusion barrier is high enough to prevent aggregation, which is due to the kinetic stability of SACs.[53–55] As shown in Fig. 2d, the values of $\Delta E_{bind} - \Delta E_{coh}$ are −0.50, −0.75, and −0.34 eV for Ti, Zr and Hf, respectively, indicating their spontaneous dispersion in the cavities of g-C₃N₄. For the other transition metals, their values are slightly higher, indicating the risk of clustering on g-C₃N₄. The diffusion barriers of Mn, Mo, Ru, W, Re, Ir and Pt were examined by CI-NEB because of their very positive ΔE_{bind} −

Fig. 2 (a) Average bond length (d_{ave}) between the TM and N atoms. (b) Deviation degree (ε) between the TM atoms and the centre of the cavity. (c) Binding energies of the TM atoms on g-C₃N₄, and (d) comparison with the corresponding cohesive energies.

This journal is © The Royal Society of Chemistry 2020

J. Mater. Chem. A, 2020, **8**, 6555–6563 | **6557**

ΔE_{coh} values (>~3 eV). As listed in Table S4,† the energy barriers are as high as 2.48, 2.67, 2.11, 3.50, 2.54, 2.30 and 1.93 eV for Mn, Mo, Ru, W, Re, Ir and Pt, respectively. These large energy barriers suggest that these single TM atoms can remain in the cavity of g-C$_3$N$_4$ steadily.

Furthermore, the binding energy of the dimer TM was calculated. As shown in Table S5,† the ΔE_{bind} values are more negative than ΔE_{bind2} for Mn, Mo, Ru, W, Re, Ir and Pt. Thus, single TM atoms are reasonably stable on the g-C$_3$N$_4$ substrate owing to the difficult formation of dimer TM. In addition, the AIMD simulation was performed at 500 K for 10 ps to illustrate their thermal stability. As seen in Fig. S3,† the energy and temperature oscillate within small ranges for Mn, Mo, Ru, W, Re, Ir and Pt/g-C$_3$N$_4$ during the period of AIMD simulation. Furthermore, these systems undergo further structural relaxation after the AIMD, and the final relaxed structures are almost the same with the initial structures. Hence, it is believed that TM/g-C$_3$N$_4$ will show high stability in real applications, in agreement with the observation in experiments.[25,27]

Bader charge analysis was conducted to gain insight into the valence states of the TM atoms (Fig. 3). The charge transfer from the TM atom to g-C$_3$N$_4$ leaves the TM atoms with positive charges, indicating a strong interaction between the TM atoms and g-C$_3$N$_4$. The amount of charge transfer decreases from left to right in each period, in good agreement with the trend of electronegativity. Hf possesses a charge transfer of 1.81e with the lowest electronegativity of 1.30, while the charge transfer of Au is reduced to 0.47e, and its electronegativity is 2.40. Furthermore, the positive charges on the TM atoms are beneficial for adsorbing ORR intermediates, which can effectively promote the ORR.

3.2 Adsorption of ORR species on TM/g-C$_3$N$_4$

The adsorption of O$_2$ on the catalyst is the first step for the effective ORR. Thus, we have examined the adsorption of O$_2$ on TM/g-C$_3$N$_4$ by considering the side-on and end-on configurations. Taking Ti and Au as examples, the side-on configuration

Fig. 3 Charge transfer (blue) and electronegativities (yellow) of the TM atoms.

of O$_2$ adsorbed on Ti/g-C$_3$N$_4$ and the end-on configuration of O$_2$ adsorbed on Au/g-C$_3$N$_4$ are shown in Fig. S4.† Apparently, O$_2$ prefers the end-on configuration with weaker adsorption on Cu, Ag and Au/g-C$_3$N$_4$, while the side-on configuration of O$_2$ is more favourable on the other TM/g-C$_3$N$_4$. The adsorption energies and bond lengths of O$_2$ on all the TM/g-C$_3$N$_4$ are listed in Table S6.† The adsorption energies of O$_2$ range from −4.80 to −0.46 eV with the TM–O bond lengths ranging from 1.79 to 2.14 Å. In addition, compared with Cu, Ag, and Au/g-C$_3$N$_4$, the distances of the O–O bond are longer for the other TM/g-C$_3$N$_4$, signifying that the O$_2$ molecule is readily dissociated.

Combined with the TM atoms, OOH, O and OH are strongly adsorbed on the substrates. The adsorption energies and bond lengths of the various ORR intermediates (OOH, O, OH and H$_2$O) are shown in Table S7–S10.† It should be noted that OOH dissociates into O and OH when absorbed on Ti, V, Zr, Nb, Mo, Hf, Re, and W/g-C$_3$N$_4$ because of the quite strong absorption of O and OH, indicating that they may not have good ORR performances. The configurations of the dissociated OOH adsorbed on Ti/g-C$_3$N$_4$ and undissociated OOH adsorbed on Au/g-C$_3$N$_4$ are shown in Fig. S5† as examples. There is a nearly linear relationship between ΔE_{*O} and ΔE_{*OH} as well as between ΔE_{*OOH} and ΔE_{*OH}, as seen in Fig. 4. ΔE_{*O} can be expressed as a function of ΔE_{*OH} by $\Delta E_{*O} = 2.40\Delta E_{*OH} + 2.06$, with a coefficient of determination (R^2) of 0.84. Similarly, the correlation between ΔE_{*OOH} and ΔE_{*OH} can be described as $\Delta E_{*OOH} = 0.89\Delta E_{*OH} + 3.16$ and $\Delta E_{*OOH} = 0.72\Delta E_{*OH} − 1.37$ for the undissociated and dissociated OOH with R^2 equals 0.94 for both cases. This result validates the previous study on metals[56] and graphene,[57] again demonstrating that catalysts possessing strong adsorption of OH are likely to show strong adsorption of O and OOH. Different from the OOH, O and OH above, with adsorption energies lower than −1.00 eV, the adsorbed H$_2$O cannot bind tightly to most of the substrates, thus H$_2$O can easily drift away from the TM/g-C$_3$N$_4$ surfaces, which guarantees the recovery of the catalysts.

To prove the reliability of using a unit cell of g-C$_3$N$_4$, the adsorption energies of the OOH, O, and OH intermediates on a 2 × 2 × 1 g-C$_3$N$_4$ supercell with a single Pd atom are listed in Table S11† and compared with a g-C$_3$N$_4$ unit cell. The results show a negligible difference between the 2 × 2 × 1 supercell and unit cell of g-C$_3$N$_4$, indicating that it is acceptable to use a unit cell of g-C$_3$N$_4$.

3.3 Evaluation of ORR performance

In general, there are two pathways for the ORR process, the four-electron pathway and the two-electron pathway, distinguished by the final product of H$_2$O or H$_2$O$_2$, respectively.[58] By examining the adsorption of H$_2$O$_2$ on TM/g-C$_3$N$_4$, we found that H$_2$O$_2$ cannot be stably absorbed on TM/g-C$_3$N$_4$. Based on this, the two-electron pathway is excluded, and the four-electron pathway is the preferred to process on TM/g-C$_3$N$_4$ in an acid environment. The four steps in detail are: (1) O$_2$ adsorbing on the surface of TM/g-C$_3$N$_4$ and reacting with H$^+$ to form *OOH; (2) *OOH reacting with H$^+$ and generating H$_2$O and *O; (3) *O combining with H$^+$ and forming *OH; and (4) the final product

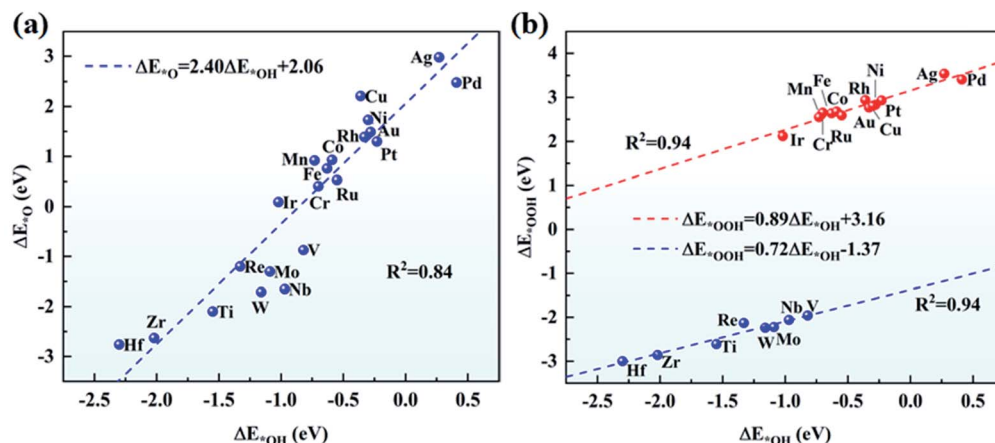**6558** | *J. Mater. Chem. A*, 2020, **8**, 6555–6563

This journal is © The Royal Society of Chemistry 2020

Fig. 4 Scaling relationship (a) between ΔE_{*O} and ΔE_{*OH}, and (b) between ΔE_{*OOH} and ΔE_{*OH} on TM/g-C$_3$N$_4$.

of H$_2$O and the H$_2$O molecule being released from the TM/g-C$_3$N$_4$ surface.

The free energy of each reaction step was calculated for all the TM/g-C$_3$N$_4$ catalysts to obtain the PDS and overpotentials. The overpotentials for all the TM supported on g-C$_3$N$_4$ are summarized in Fig. 5a. Nørskov and co-workers illustrated that the ORR overpotential of Pt(111) is 0.45 V, which is close to the experimental observation.[56] The overpotentials of Pd/g-C$_3$N$_4$ and Ag/g-C$_3$N$_4$ are 0.46 V and 0.60 V, respectively, which are close to that of Pt(111), indicating that they are potential substitutes of Pt(111), especially Pd/g-C$_3$N$_4$. Moreover, the 0.46 V overpotential value for Pd/g-C$_3$N$_4$ is lower than that in previous studies, such as Fe-Pc (0.68 V),[59] Fe-Pp (0.77 V),[60] CoN$_4$-gra (0.47 V)[61] and Co/BN (0.82 V),[62] proving a better ORR

performance with g-C$_3$N$_4$ as the support. The free energy changes in each step on all the TM/g-C$_3$N$_4$ are shown in Table S12.† Obviously, the PDS is the last step for most of the TM/g-C$_3$N$_4$, except for V (the second step, from *OOH to *O), Nb and W/g-C$_3$N$_4$ (the third step, from *O to *OH). The free energy diagrams of Pd/g-C$_3$N$_4$ are shown in Fig. 5b, and that of the other TM atoms supported on g-C$_3$N$_4$ are shown in Fig. S6–S8† for clarity. Obviously, the diagrams of Ti, V, Zr, Nb, Mo, Hf, W and Re/g-C$_3$N$_4$ are different from the other TM/g-C$_3$N$_4$ because of the dissociated OOH, which leads to a high overpotential. The structures of the ORR intermediates (O$_2$, OOH, O, OH and H$_2$O) adsorbed on Pd/g-C$_3$N$_4$ can be found in Fig. 5c. However, besides Pd/g-C$_3$N$_4$ and Ag/g-C$_3$N$_4$, none of the remaining TM/g-C$_3$N$_4$ have catalytic ORR activity because of their large
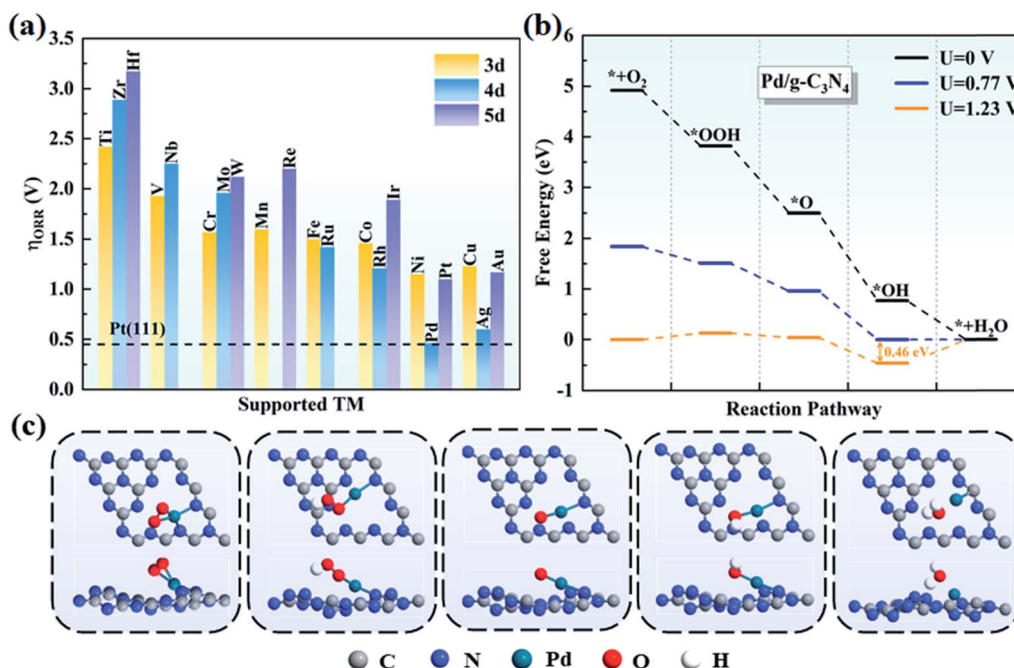

Fig. 5 (a) Summary of the ORR overpotentials for TM supported on g-C$_3$N$_4$. (b) Free energy diagrams for the ORR on Pd/g-C$_3$N$_4$ and (c) corresponding atomic configurations of ORR species on Pd/g-C$_3$N$_4$.

This journal is © The Royal Society of Chemistry 2020
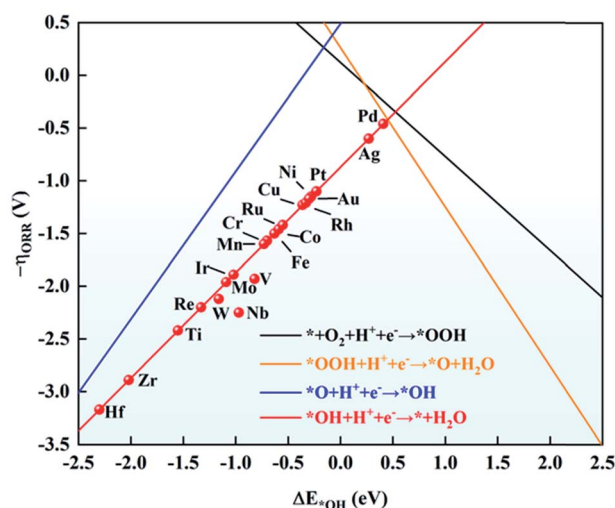
J. Mater. Chem. A, 2020, **8**, 6555–6563 | **6559**

Fig. 6 Relationship between the negative of overpotential ($-\eta_{ORR}$) and the adsorption energy of OH (ΔE_{*OH}). Each line denotes one reaction step acquired from the scaling relationships, $* + O_2 + H^+ + e^- \rightarrow *OOH$ (in black): $-\eta_{ORR} = -0.89\Delta E_{*OH} + 0.12$; $*OOH + H^+ + e^- \rightarrow *O + H_2O$ (in yellow): $-\eta_{ORR} = -1.51\Delta E_{*OH} + 0.26$; $*O + H^+ + e^- \rightarrow *OH$ (in blue): $-\eta_{ORR} = 1.40\Delta E_{*OH} + 0.49$; $*OH + H^+ + e^- \rightarrow * + H_2O$ (in red): $-\eta_{ORR} = \Delta E_{*OH} - 0.87$.

overpotential of more than 1.00 V. Thus, these catalysts were not further considered as potential ORR catalysts.

As mentioned above, the adsorption energies of OH have a scaling relationship with OOH and O. Based on this, ΔE_{*OH} was chosen as a descriptor to explore the ORR activity on TM/g-C$_3$N$_4$. The relationship between the negative ORR overpotential ($-\eta_{ORR}$)

and ΔE_{*OH} is established in Fig. 6. According to the Sabatier principle,[63] intermediates adsorbed on the TM too strongly and too weakly can both discourage the catalytic process. The intermediates will poison the electrode surface if they are adsorbed too strongly, thus the proton–electron cannot transfer from TM to the intermediates. However, the results revealed the strong adsorption of the ORR species on TM/g-C$_3$N$_4$, indicating the risk of deactivation. Among the TM/g-C$_3$N$_4$, Pd/g-C$_3$N$_4$ is the closest to the top of the volcano plot, where the lowest ORR overpotential was calculated to be 0.42 V, suggesting that it is the closest catalyst to the theoretical minimum of the ORR overpotential.

3.4 Origin of ORR activity trend

To better understand the origin of the ORR activity trend, we chose the 4d metals, where Pd and Ag are included, for comprehensive analysis. During the catalytic process, the adsorption strength of intermediates can be modulated by different TM atoms supported on g-C$_3$N$_4$. Taking the adsorption of OH as an example, the adsorption strength between OH and TM on TM/g-C$_3$N$_4$ can be demonstrated by the bond formation, as illustrated in Fig. S9.† To reveal the role of the different TM centres, the d-band centre (ε_d) of TM/g-C$_3$N$_4$ was calculated as follows:[64]

$$\varepsilon_d = \frac{\int_{-\infty}^{\infty} \varepsilon \rho_d d\varepsilon}{\int_{-\infty}^{\infty} \rho_d d\varepsilon} \qquad (7)$$

where ρ_d is the density of states projected onto a single TM atom d orbital and ε is the energy width of the d orbital.
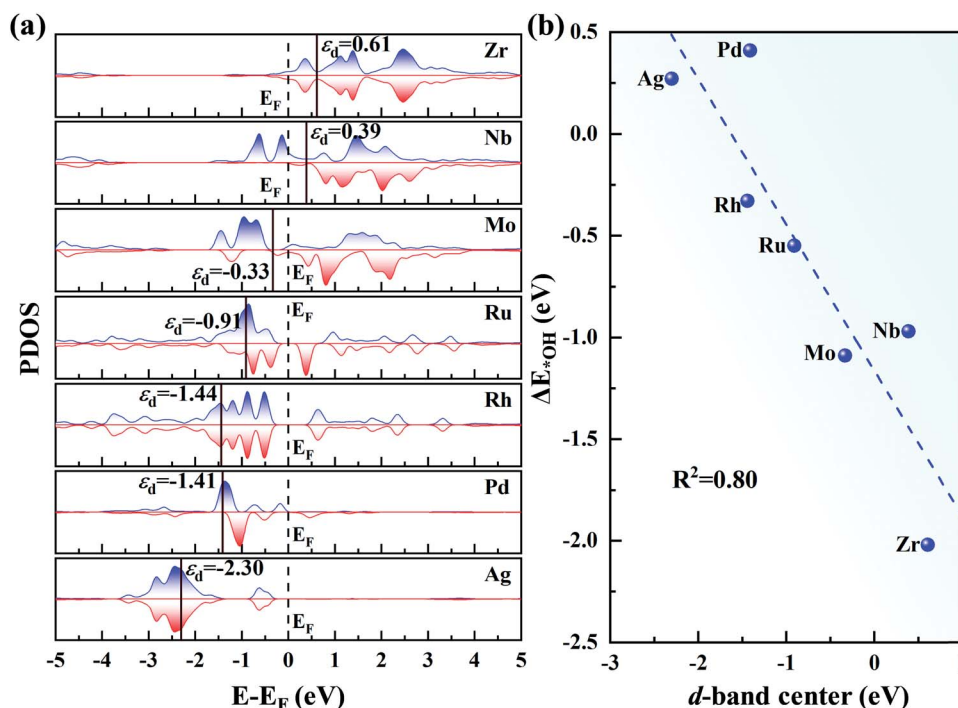

Fig. 7 (a) Partial density of states of the 4d TM atoms on g-C$_3$N$_4$, where E_F denotes the Fermi level and is set to zero. (b) Relationship between the d-band centre of TM/g-C$_3$N$_4$ and ΔE_{*OH}.

6560 | *J. Mater. Chem. A*, 2020, **8**, 6555–6563

This journal is © The Royal Society of Chemistry 2020

In Fig. 7a, as the d orbital occupation increases, ε_d of the 4d TM atoms become more negative relative to the Fermi level (E_F). A more negative ε_d usually implies weaker adsorption of the ORR species. Thus, the positive ε_d of Zr and Nb indicate the strong adsorption of the intermediates. However, for Mo, Ru, Rh, Pd and Ag, ε_d shifts to the left of E_F, and thus the adsorption of the intermediates become weaker. The relationship between ε_d and ΔE_{*OH} is presented in Fig. 7b. The good correlation coefficient ($R^2 = 0.80$) indicates that the d-band centre can serve as a great descriptor to accurately illustrate the trend of ΔE_{*OH} on TM/g-C$_3$N$_4$. However, the d-band center is not associated with the adsorption energy for a specific TM in a small range due to the neglect of the d-band shape and the effect of the TM-sp orbitals (Fig. S10†).[65,66]

pCOHP was employed to analyse the bonding and anti-bonding states of the OH intermediate absorbed on the TM centre. From Zr to Ag, there is a trend that the filling of the antibonding orbital population increases and the energies of the bonding states move up to E_F, in accordance with the variation in adsorption strength of the intermediates. To give a more quantitative explanation, the integrated COHP (ICOHP) was calculated by integrating the energy up to E_F. Interestingly, there is a good linear relationship between ICOHP and ΔE_{*OH} values (with $R^2 = 0.89$, Fig. 8h). This linear correlation quantitatively reveals the role of different metal centres in the

bonding/antibonding orbital populations, which accounts for the observed trend of ΔE_{*OH} above.

Although both the d-band centre and pCOHP explain the origin of the ORR activity trend well, it is still to be solved whether a better descriptor can be found to give an easier and more thorough explanation and even predict the ORR activity. Considering that the charge transfer of TM has been used to prove the performance of SAC,[67] the relationship between the Bader charge transfer of the TM and the OH adsorption energy was further explored. As seen in Fig. 9a, Zr with the most positive charge of 1.74e shows the largest ΔE_{*OH} of −2.02 eV among the 4d metals, while Pd loses 0.42e with the ΔE_{*OH} of 0.41 eV. There is a linear relationship between the charge transfer of the TM and the OH adsorption energy with a fine correlation coefficient ($R^2 = 0.88$), indicating that a more positive charge on the TM atom leads to more strongly adsorbing ORR intermediates, which gives evidence of the ORR origin from a new point of view.

Furthermore, inspired by the recent study of a universal descriptor to predict the ORR/OER/HER activities for graphene-based SACs,[45] the descriptor φ to predict the ORR activities of TM/g-C$_3$N$_4$ considering the number of d orbital electron (θ_d) and the electronegativity of TM (E_{TM}) is proposed as follows:

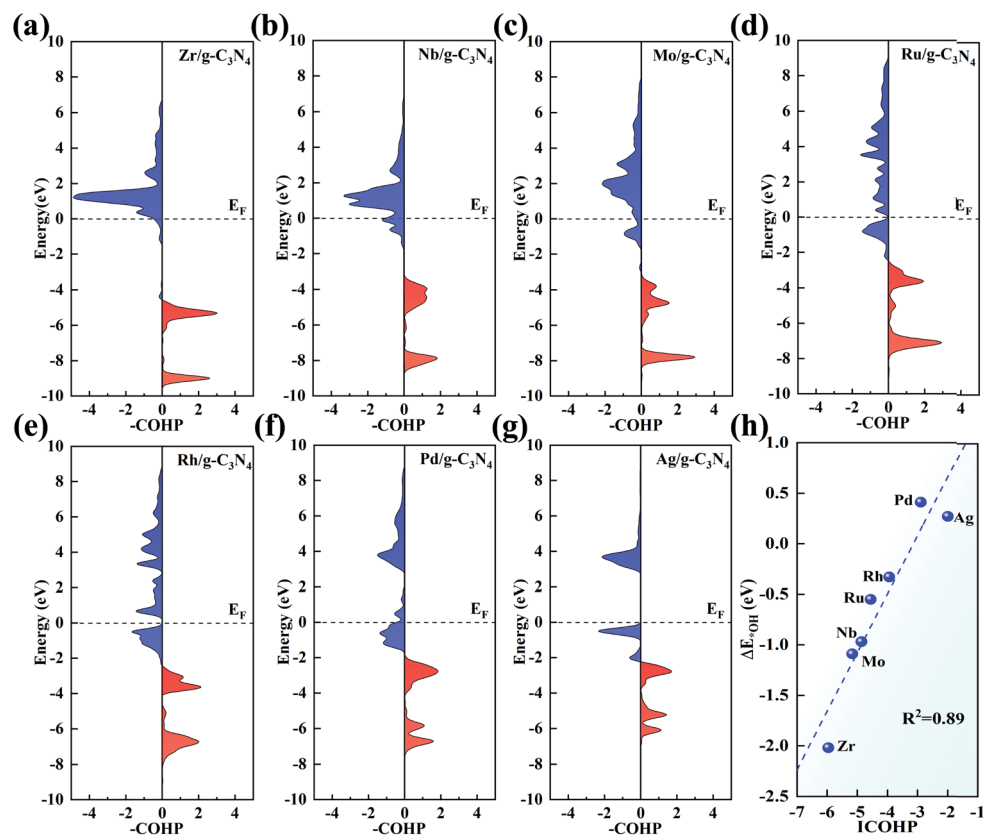$$\varphi = \theta_d \times E_{TM} \tag{8}$$

Fig. 8 (a–g) pCOHP between the 4d TM centres (from Zr to Ag) and the OH intermediate. The bonding and antibonding contributions are displayed on the right and left, respectively. (h) Correlation between ICOHP and the adsorption energy of the OH intermediate.
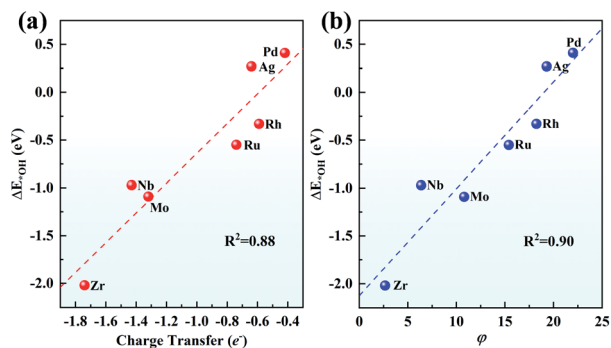
This journal is © The Royal Society of Chemistry 2020

J. Mater. Chem. A, 2020, **8**, 6555–6563 | **6561**

Fig. 9 Relationship (a) between the charge transfer and ΔE_{*OH} and (b) between φ and ΔE_{*OH}.

As shown in Fig. 9b, with θ_d multiplied by E_{TM}, φ correlates linearly with ΔE_{*OH} quite well with $R^2 = 0.90$. This indicates that the adsorption strength of OH and the other intermediates can be easily estimated by basic characteristics rather than complex DFT calculations.

Moreover, we investigated all the TM screened in our study to evaluate whether these descriptors can be applied more broadly. As shown in Fig. S11,† there is a linear relationship for ΔE_{*OH} *versus* d-band center, ICOHP, charge transfer and φ with $R^2 = 0.67, 0.77, 0.73$ and 0.69, respectively. Thus, our results validate these descriptors can be used not only in a period but also for all TM. As shown in Fig. 10, on one hand, ΔE_{*OH} can serve as a facial descriptor of ORR activity; on the other hand, ε_d, ICOHP, Bader charge transfer and φ give a quantitative description of ΔE_{*OH}. Hence, it is systematically concluded that the ORR activity is intrinsically determined by the φ of TM atoms. The different φ leads to a different positive charge of TM atoms, resulting in a variation in electronic structures, such as bonding/antibonding orbital population and d-band centre. The electronic structures can further impact the adsorption strength of intermediates and reflect the ORR activity.
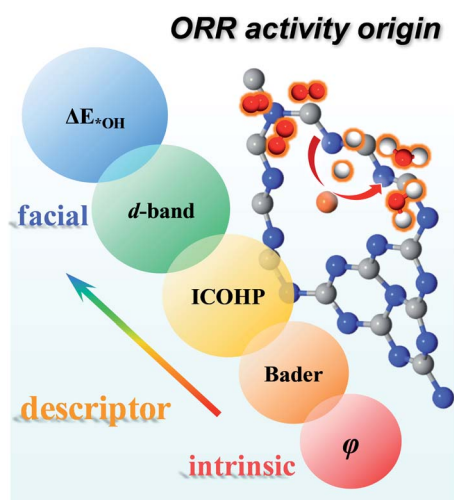

Fig. 10 Descriptors of the ORR activity origin, including ΔE_{*OH}, d-band centre, ICOHP, Bader charge transfer and φ.

4. Conclusions

In conclusion, we revealed that single transition metal atoms supported on g-C$_3$N$_4$ can serve as promising high activity catalysts for the ORR by means of systematic first-principles calculations. Our detailed screening of a series of TM elements indicates that TM single atoms and g-C$_3$N$_4$ strongly combine, with charge transfer from the TM atoms toward g-C$_3$N$_4$. With a favourable ORR overpotential of 0.46 V, Pd/g-C$_3$N$_4$ demonstrates the highest performance among the TM/g-C$_3$N$_4$. Therefore, it is a potential competitive candidate for replacing the noble Pt catalyst. Furthermore, based on the scaling relationship between the adsorption energy of the ORR intermediates, ΔE_{*OH} can serve as an energy descriptor to reflect the ORR activity of TM/g-C$_3$N$_4$. The variation trend of ΔE_{*OH} on TM/g-C$_3$N$_4$ can be properly described by the d-band center, ICOHP and charge transfer. An intrinsic descriptor φ involving θ_d and E_{TM} can be applied to predict the ORR activity. The multiple-level descriptors including basic characteristics, charge transfer, electronic structures and energy will provide greater insight to reveal the ORR activity mechanisms and improving the ORR activities of SACs.

Conflicts of interest

There are no conflicts to declare.

Acknowledgements

References

1 M. Winter and R. J. Brodd, *Chem. Rev.*, 2004, **104**, 4245–4270.

2 W. Xia, A. Mahmood, Z. Liang, R. Zou and S. Guo, *Angew. Chem., Int. Ed.*, 2016, **55**, 2650–2676.

3 Y. Jiao, Y. Zheng, M. Jaroniec and S. J. Qiao, *J. Am. Chem. Soc.*, 2014, **136**, 4394–4403.

4 V. R. Stamenkovic, B. S. Mun, M. Arenz, K. J. Mayrhofer, C. A. Lucas, G. Wang, P. N. Ross and N. M. Markovic, *Nat. Mater.*, 2007, **6**, 241.

5 N. Tian, Z. Zhou, S. Sun, Y. Ding and Z. Wang, *Science*, 2007, **316**, 732–735.

6 C. Wang, H. Daimon, T. Onodera, T. Koda and S. Sun, *Angew. Chem., Int. Ed.*, 2008, **47**, 3588–3591.

7 J. Wu and H. Yang, *Acc. Chem. Res.*, 2013, **46**, 1848–1857.

8 A. Brouzgou, S. Song and P. Tsiakaras, *Appl. Catal., B*, 2012, **127**, 371–388.

9 W. Liang, J. Chen, Y. Liu and S. Chen, *ACS Catal.*, 2014, **4**, 4170–4177.

10 X. Zhao, X. Liu, B. Huang, P. Wang and Y. Pei, *J. Mater. Chem. A*, 2019, **7**, 24583–24593.

11 B. Qiao, A. Wang, X. Yang, L. F. Allard, Z. Jiang, Y. Cui, J. Liu, J. Li and T. Zhang, *Nat. Chem.*, 2011, **3**, 634.

12 T. K. Ghosh and N. N. Nair, *ChemCatChem*, 2013, **5**, 1811–1821.

6562 | *J. Mater. Chem. A*, 2020, **8**, 6555–6563

This journal is © The Royal Society of Chemistry 2020

13 P. Liu, Y. Zhao, R. Qin, S. Mo, G. Chen, L. Gu, D. M. Chevrier, P. Zhang, Q. Guo and D. Zang, *Science*, 2016, **352**, 797–800.

14 J. Jones, H. Xiong, A. T. DeLaRiva, E. J. Peterson, H. Pham, S. R. Challa, G. Qi, S. Oh, M. H. Wiebenga and X. I. P. Hernández, *Science*, 2016, **353**, 150–154.

15 B. Zhang, T. Fan, N. Xie, G. Nie and H. Zhang, *Adv. Sci.*, 2019, **6**, 1901787.

16 K. C. Kwon, J. M. Suh, R. S. Varma, M. Shokouhimehr and H. W. Jang, *Small Methods*, 2019, **3**, 1800492.

17 Y. Zhu, W. Sun, J. Luo, W. Chen, T. Cao, L. Zheng, J. Dong, J. Zhang, M. Zhang and Y. Han, *Nat. Commun.*, 2018, **9**, 3861.

18 H. Yu, Y. Xue, B. Huang, L. Hui, C. Zhang, Y. Fang, Y. Liu, Y. Zhao, Y. Li and H. Liu, *iScience*, 2019, **11**, 31–41.

19 Y. Zhou, G. Gao, J. Kang, W. Chu and L. W. Wang, *J. Mater. Chem. A*, 2019, **7**, 12050–12059.

20 N. Xuan, J. Chen, J. Shi, Y. Yue, P. Zhuang, K. Ba, Y. Sun, J. Shen, Y. Liu and B. Ge, *Chem. Mater.*, 2018, **31**, 429–435.

21 X. Wang, K. Maeda, A. Thomas, K. Takanabe, G. Xin, J. M. Carlsson, K. Domen and M. Antonietti, *Nat. Mater.*, 2009, **8**, 76–80.

22 X. Zhang, T. Peng, L. Yu, R. Li, Q. Li and Z. Li, *ACS Catal.*, 2014, **5**, 504–510.

23 P. Huang, J. Huang, S. A. Pantovich, A. D. Carl, T. G. Fenton, C. A. Caputo, R. L. Grimm, A. I. Frenkel and G. Li, *J. Am. Chem. Soc.*, 2018, **140**, 16042–16047.

24 S. Ohn, S. Y. Kim, S. K. Mun, J. Oh, Y. J. Sa, S. Park, S. H. Joo, S. J. Kwon and S. Park, *Carbon*, 2017, **124**, 180–187.

25 S. Tian, Z. Wang, W. Gong, W. Chen, Q. Feng, Q. Xu, C. Chen, C. Chen, Q. Peng and L. Gu, *J. Am. Chem. Soc.*, 2018, **140**, 11161–11164.

26 E. Vorobyeva, Z. Chen, S. Mitchell, R. K. Leary, P. Midgley, J. M. Thomas, R. Hauert, E. Fako, N. López and J. Pérez-Ramírez, *J. Mater. Chem. A*, 2017, **5**, 16393–16403.

27 X. Li, W. Bi, L. Zhang, S. Tao, W. Chu, Q. Zhang, Y. Luo, C. Wu and Y. Xie, *Adv. Mater.*, 2016, **28**, 2427–2431.

28 G. Gao, Y. Jiao, E. R. Waclawik and A. Du, *J. Am. Chem. Soc.*, 2016, **138**, 6292–6297.

29 S. L. Li, H. Yin, X. Kan, L. Y. Gan, U. Schwingenschlögl and Y. Zhao, *Phys. Chem. Chem. Phys.*, 2017, **19**, 30069–30077.

30 Z. Chen, J. Zhao, C. R. Cabrera and Z. Chen, *Small Methods*, 2018, **3**, 1800368.

31 F. He, K. Li, C. Yin, Y. Wang, H. Tang and Z. Wu, *Carbon*, 2017, **114**, 619–627.

32 X. Chen and R. Hu, *Int. J. Hydrogen Energy*, 2019, **44**, 15409–15416.

33 G. Kresse and J. Furthmüller, *Comput. Mater. Sci.*, 1996, **6**, 15–50.

34 P. E. Blöchl, *Phys. Rev. B: Condens. Matter Mater. Phys.*, 1994, **50**, 17953.

35 J. P. Perdew, K. Burke and M. Ernzerhof, *Phys. Rev. Lett.*, 1996, **77**, 3865.

36 J. Zhou and Q. Sun, *J. Am. Chem. Soc.*, 2011, **133**, 15113–15119.

37 X. Zhang, Z. Bao, X. Ye, W. Xu, Q. Wang and Y. Liu, *Nanoscale*, 2017, **9**, 11231.

38 S. Grimme, *J. Comput. Chem.*, 2006, **27**, 1787–1799.

39 W. Tang, E. Sanville and G. Henkelman, *J. Phys.: Condens. Matter*, 2009, **21**, 084204.

40 G. Henkelman, B. P. Uberuaga and H. Jónsson, *J. Chem. Phys.*, 2000, **113**, 9901.

41 S. Nosé, *J. Chem. Phys.*, 1984, **81**, 511–519.

42 R. Dronskowski and P. E. Blöchl, *J. Phys. Chem.*, 1993, **97**, 8617–8624.

43 V. L. Deringer, A. L. Tchougréeff and R. Dronskowski, *J. Phys. Chem. A*, 2011, **115**, 5461–5466.

44 S. Maintz, V. L. Deringer, A. L. Tchougréeff and R. Dronskowski, *J. Comput. Chem.*, 2016, **37**, 1030–1035.

45 V. Wang, N. Xu, J. C. Liu, G. Tang and W. Geng, 2019, arXiv: 1908.08269.

46 I. C. Man, H. Y. Su, F. Calle-Vallejo, H. A. Hansen, J. I. Martínez, N. G. Inoglu, J. Kitchin, T. F. Jaramillo, J. K. Nørskov and J. Rossmeisl, *ChemCatChem*, 2011, **3**, 1159–1165.

47 J. K. Nørskov, T. Bligaard, A. Logadottir, J. Kitchin, J. G. Chen, S. Pandelov and U. Stimming, *J. Electrochem. Soc.*, 2005, **152**, J23–J26.

48 H. Xu, D. Cheng, D. Cao and X. C. Zeng, *Nat. Catal.*, 2018, **1**, 339.

49 H. Z. Wu, L. M. Liu and S. J. Zhao, *Phys. Chem. Chem. Phys.*, 2014, **16**, 3299–3304.

50 Q. Gao, S. Hu, Y. Du and Z. Hu, *J. Mater. Chem. A*, 2017, **5**, 4827–4834.

51 Y. Zheng, Y. Jiao, Y. Zhu, Q. Cai, A. Vasileff, L. H. Li, Y. Han, Y. Chen and S. Z. Qiao, *J. Am. Chem. Soc.*, 2017, **139**, 3336–3339.

52 H. Li, Y. Wu, L. Li, Y. Gong, L. Niu, X. Liu, T. Wang, C. Sun and C. Li, *Appl. Surf. Sci.*, 2018, **457**, 735–744.

53 J. C. Liu, Y. Tang, Y. Wang, T. Zhang and J. Li, *Natl. Sci. Rev.*, 2018, **5**, 638–641.

54 C. Liu, Q. Li, J. Zhang, Y. Jin, D. R. MacFarlane and C. Sun, *J. Mater. Chem. A*, 2019, **7**, 4771–4776.

55 X. Lv, W. Wei, H. Wang, B. Huang and Y. Dai, *Appl. Catal., B*, 2020, **264**, 118521.

56 J. K. Nørskov, J. Rossmeisl, A. Logadottir, L. Lindqvist, J. R. Kitchin, T. Bligaard and H. Jonsson, *J. Phys. Chem. B*, 2004, **108**, 17886–17892.

57 F. Calle-Vallejo, J. I. Martinez and J. Rossmeisl, *Phys. Chem. Chem. Phys.*, 2011, **13**, 15639–15643.

58 A. Kulkarni, S. Siahrostami, A. Patel and J. K. Nørskov, *Chem. Rev.*, 2018, **118**, 2302–2312.

59 Y. Wang, H. Yuan, Y. Li and Z. Chen, *Nanoscale*, 2015, **7**, 11633–11641.

60 G. Luo, Y. Wang and Y. Li, *Sci. Bull.*, 2017, **62**, 1337–1343.

61 X. Zhang, Z. Yang, Z. Lu and W. Wang, *Carbon*, 2018, **130**, 112–119.

62 C. Deng, R. He, W. Shen, M. Li and T. Zhang, *Phys. Chem. Chem. Phys.*, 2019, **21**, 6900–6907.

63 G. Rothenberg, *Catalysis: concepts and green applications*, John Wiley & Sons, 2017.

64 A. Ruban, B. Hammer, P. Stoltze, H. L. Skriver and J. K. Nørskov, *J. Mol. Catal. A: Chem.*, 1997, **115**, 421–429.

65 H. Xin, A. Vojvodic, J. Voss, J. K. Nørskov and F. Abild-Pedersen, *Phys. Rev. B: Condens. Matter Mater. Phys.*, 2014, **89**, 115114.

66 X. Liu, Y. Jiao, Y. Zheng, M. Jaroniec and S. Z. Qiao, *J. Am. Chem. Soc.*, 2019, **141**, 9664–9672.

67 L. Li, X. Wang, H. Guo, G. Yao and L. Chen, *Small Methods*, 2019, **3**, 1900337.

This journal is © The Royal Society of Chemistry 2020

J. Mater. Chem. A, 2020, **8**, 6555–6563 | **6563**